Influence of Antisite Defects in Yttrium−Aluminum Garnet on Paramagnetic Centers of Ce^{3+} and Tb^{3+}

G. R. Asatryan[a], *, E. V. Edinach[a], Yu. A. Uspenskaya[a], R. A. Babunts[a], A. G. Badalyan[a],
N. G. Romanov[a], A. G. Petrosyan[b], and P. G. Baranov[a]

[a] Ioffe Institute, St. Petersburg, 194021 Russia
[b] Institute for Physical Research, National Academy of Sciences of Armenia, Ashtarak-2, 0203 Republic of Armenia
*e-mail: hike.asatryan@mail.ioffe.ru

Abstract—In yttrium aluminum garnet (YAG) crystals containing terbium and cerium impurities, along with the main EPR signals of Tb^{3+} and Ce^{3+} ions located in the dodecahedral sites of the YAG lattice in a regular environment, EPR lines with a lower (several percent) intensity were observed. They also belong to the paramagnetic centers of terbium and cerium, but are characterized by slightly altered parameters—the initial level splitting for non-Kramers Tb^{3+} ions and g-factors for Ce^{3+} ions. It is shown that the nature of such centers and their number can be explained by the presence of Y_{Al} antisite defects, i.e. yttrium ions in the octahedral aluminum positions, in the environment of Tb^{3+} and Ce^{3+}.

INTRODUCTION

Garnet crystals activated by rare-earth ions are widely used in quantum electronics and optoelectronics, applied as scintillators in nuclear physics and medical diagnostics; they are also promising systems for quantum calculations [1−5]. Growth from melt at high temperatures can be accompanied in these crystals by appearance of permutation defects, also called antisite defects. In crystal of yttrium-aluminum garnet (YAG) $Y_3Al_5O_{12}$ they appear when Al^{3+} ions are replaced by Y^{3+} ions (situation denoted as Y_{Al}) or when Y^{3+} in dodecahedral *c*-centers is replaced by Al^{3+} (Al_Y).

Investigation [6] was one of the first dedicated to X-ray analysis of aluminum and gallium garnets, where the substitution of Y^{3+} ions for Al^{3+} or Ga^{3+} was considered. The presence of antisite defects in crystals of this type was proved in [7, 8] based on optical spectra of impurity rare-earth ions. All crystals of aluminum and gallium garnets grown from melt were shown to be nonstoichiometric due to insertion of some rare-earth ions to the positions of octahedral Al^{3+} or Ga^{3+}. Concentration of antisite defects $Y_{Al(a)}$ in YAG is about 1.5% according to the estimate made in [7]. The presence of the antisite defects in garnet crystals was explained to cause the noncubic lattice symmetry, which was revealed in the study of the extended X-ray absorption fine structure (EXAFS) [9]. Existence of the antisite defects in YAG also follows from the mea-

surements of positron annihilation and X-ray absorption spectra near the absorption band edge [10]. Direct observation of the antisite defects was made by nuclear magnetic resonance (NMR) in iron-yttrium garnet [11]. Antisite positions of yttrium ions in the lattice of perovskite crystals $YAlO_3$ were unambiguously identified from NMR spectra of ^{89}Y [12].

Theoretical calculations of the formation energy of various defects in YAG crystals showed that the antisite defects dominate among intrinsic defects since their formation energy is lower than that of Frenkel and Schottky defects [13−15]. Calculated energies of crystal lattice distortions caused by the antisite atom $Y_{Al(a)}$ are in good agreement with the results obtained by the EXAFS measurements. First-principle simulations of the atomic and electronic structure of the antisite defects in YAG based on the density functional theory were conducted in [16, 17]. According to these studies, substitution of yttrium for octahedral positions of aluminum $Y_{Al(a)}$ is the most favorable among all possible ways of insertion of additional yttrium cations in the YAG structure, and calculated concentrations of defects of this kind agree with the experimental estimates [15]. Substitution Al_Y has higher formation energy even at the excessive content of Al_2O_3, which points to a small probability of formation of defects of this type.

Antisite defects lead to formation of electron traps and influence substantially the recombination pro-

cesses and luminescence decay time in garnet-based scintillators [18, 19]. Therefore, investigations of antisite defects are important from the practical point of view, to improve scintillators based on cerium-containing garnets.

Since antisite defects are not paramagnetic, their direct observation by means of electron paramagnetic resonance (EPR) is impossible. However, a significant difference in the ionic radii ($r_{Al(6)}^{3+} = 0.53$ Å, $r_{Y(6)}^{3+} = 0.9$ Å) replacement of Al^{3+} ions by Y^{3+} should lead to a significant distortion of the crystal lattice near the paramagnetic center. Oxygen ions, belonging at the same time to the environment of the paramagnetic center and of the antisite defect, are shifted. Distortions in the nearest surrounding can thus make the effect of the antisite defects observable in the EPR spectra of the paramagnetic centers situated in the vicinity of the defect positions.

Trivalent impurity ions of rare-earths in YAG occupy usually dodecahedral c-positions of the Y^{3+} ions. Ions of Ce^{3+} were studied in YAG by EPR [20, 21]. Lines of a smaller intensity were observed in [21] together with intensive main EPR lines of Ce^{3+}; they were ascribed to cerium ions with antisite defects in their nearest environment. Similar to Y^{3+}, part of the impurity rare-earth ions may also occupy octahedral a-positions, replacing Al^{3+} ions. Optical spectra of Er^{3+} ions in the aluminum positions in YAG were observed in [7]. Paper [22] reported on EPR spectra of Ce^{3+} ions in the positions of Al^{3+} in the crystal of $Lu_3Al_5O_{12}$ (LuAG). However, cerium centers of this kind have not been found in YAG yet.

EPR of Tb^{3+} ions is of special interest for studies of antisite defects in garnet crystals. The zero-field splitting of the levels of the non-Kramers quasi-doublet is very sensitive to the symmetry of the environment and, hence, to the presence of defects near the ions. The energy of the microwave quantum should exceed the zero-field splitting of the Tb^{3+} ion, and therefore a special high-frequency spectrometer is required to observe EPR spectra. EPR spectra of Tb^{3+} in YAG at 94 and 130 GHz were obtained recently and reported in [23]. As in the case of Ce^{3+} ions, weaker EPR lines were also observed and assigned to the terbium paramagnetic centers with altered parameters.

The present work is dedicated to the study of high-frequency EPR spectra of paramagnetic centers of terbium and cerium in YAG:Ce, Tb crystals and to analysis of the influence of the antisite defects located near these ions on the spectral parameters.

EXPERIMENTAL

Single crystals of $Y_3Al_5O_{12}$:Ce, Tb grown at 1940°C in molybdenum containers by vertical directed crystallization were studied [24, 25]; crystallization was car-

ried out in the Institute for Physical Research of the National Academy of Sciences of Armenia (Ashtarak, Armenia). Cerium content was 0.1 at % relative to yttrium. Estimates showed that the terbium concentration was about 0.01%. The crystals were grown along the crystallographic axis ⟨100⟩. The lattice parameter a on the [211] facets is bigger than in the bulk material ($\Delta a/a = 1.3 \times 10^{-4}$) [26, 27], which is due to the difference of the growth mechanisms [28] leading to the different concentrations of the antisite defects $Y_{Al(a)}$. For example, the concentration of the antisite defects Lu_{Al} in LuAG was estimated from the increase of the lattice parameters to be about 1.2% in the volume and 2.7% on the facets [29, 30]. Samples used in the present study were cut from the uniform middle regions of the obtained crystals.

EPR spectra at the frequencies of 94 and 130 GHz were recorded at the temperatures from 1.5 to 40 K using a high-frequency EPR-ODMR spectrometer developed in Ioffe Institute, which is described in [23, 31]. EPR measurements at 9 GHz were carried out at the temperatures from 4.2 to 40 K on a JEOL radiospectrometer equipped with an ESR900 helium cryostat.

RESULTS AND DISCUSSION

Figure 1a shows energy levels of the ground state of Tb^{3+} ions in YAG and EPR transitions at the frequencies of 94 and 130 GHz with the crystal orientation **B** ∥ [100]. The EPR spectra obtained at the given frequencies are shown in Fig. 1b. Terbium has one stable isotope ^{159}Tb (natural abundance 100%) with the nuclear spin of $I = 3/2$, and hence the EPR spectrum contains four equidistant lines of the hyperfine structure. The EPR spectrum at 94 GHz contains signals near zero magnetic field. They correspond to the terbium ions whose zero-field splitting Δ is close to the energy of the microwave quantum at 94 GHz. The EPR spectrum at 130 GHz contains also lines nearly 50 times weaker than the main quartet of Tb^{3+}; these weak lines show a clear hyperfine structure typical of terbium ions.

The electron structure of terbium ion Tb^{3+} is $4f^8$; the ground state, according to the Hund's rule, is $^7F_6$ ($L = 3$, $S = 3$, $J = 6$). In the axial-symmetric crystalline field the ground state is split into six doublets with $M_J = \pm 6, \pm 5, ..., \pm 1$ and a singlet with $M_J = 0$ [32]. The doublet with $M_J = \pm 6$ is the lowest-energy. Admixture of excited states by the crystalline field splits this peak into a doublet in zero field and decreases the value of $g_\parallel$ compared with the value of 18 corresponding to the pure state with $M_J = \pm 6$.

Tb^{3+} EPR spectra can be described by the effective spin Hamiltonian for a non-Kramers quasi-doublet
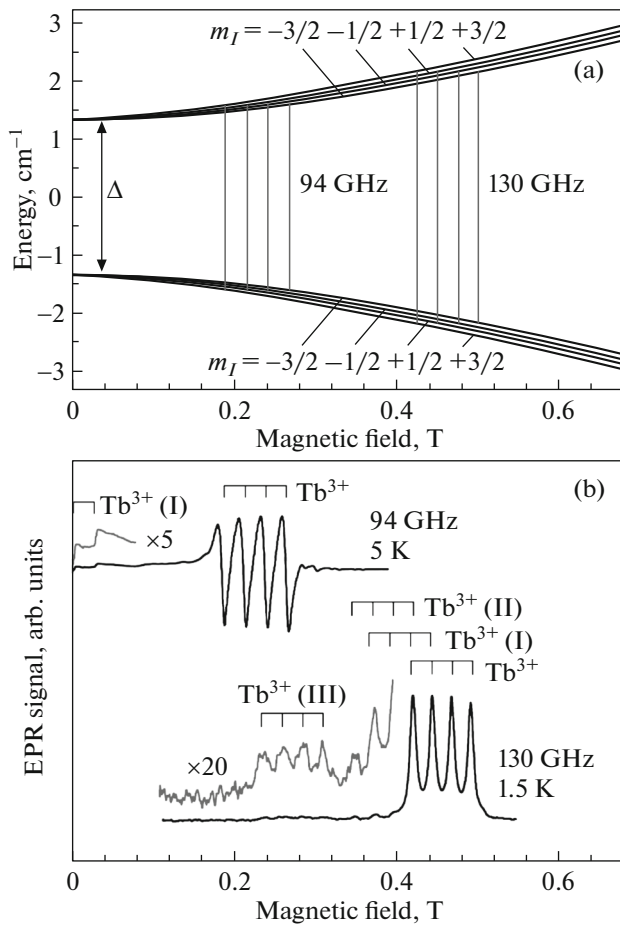
Fig. 1. (a) Energy levels of Tb^{3+} ions in YAG and EPR transitions (vertical lines) at the frequencies of 94 and 130 GHz at the crystal orientation **B** ∥ [100]. (b) EPR spectra obtained at $T = 5$ K at 94 GHz and at 1.5 K at the frequency of 130 GHz in YAG:Ce, Tb. Crystal orientation is **B** ∥ [100]. The hyperfine quartets of the main terbium centers and the additional centers Tb^{3+}(I), Tb^{3+}(II), and Tb^{3+}(III) are shown. EPR lines of Tb^{3+}(I) with $\Delta \approx$ 94 GHz overlap with the signals of Tb^{3+} and Tb^{3+}(II).

with the effective electron spin of $S^* = 1/2$ and nuclear spin of $I = 3/2$ [33]:

$$\hat{H} = \mu_B \mathbf{S} \cdot \mathbf{g} \cdot \mathbf{B} + (\Delta_x S_x + \Delta_y S_y) + A S_z I_z, \qquad (1)$$

where μ_B is the Bohr magneton and $S = 1/2$ is the effective electron spin. The first term in Eq. (1) describes the Zeeman interaction; the second term

Table 1. Parameters of terbium centers in the YAG crystal

Center	$g_\parallel$	Δ, GHz	A, GHz
Tb^{3+}	15.7	81.09	6.41
Tb^{3+}(I)	15.8	93.94	6.41
Tb^{3+}(II)	15.8	98.03	6.41
Tb^{3+}(III)	15.6	115.1	6.41

describes splitting of electron levels in the zero magnetic field, $\Delta = (\Delta_x^2 + \Delta_y^2)^{1/2}$; the last term is the hyperfine interaction characterized by the constant A.

Energy levels of Tb^{3+} in the magnetic field are given by the following expression:

$$W = \pm \frac{1}{2} \sqrt{\Delta^2 + (g_z \mu_B B_z + A I_z)^2}, \qquad (2)$$

where g_z is the component of g factor along the z axis. Other components $g_\perp = g_x = g_y = 0$ for Tb^{3+}. Principal local magnetic axes of the paramagnetic terbium centers were chosen so that the axis z was parallel to one of the directions $\langle 100 \rangle$, and the axes x and y coincided with the directions $\langle 110 \rangle$.

The degree at which the degeneracy of the doublet of the ground state of Tb^{3+} is removed (i.e., the zero-field splitting Δ) depends strongly on the crystalline field [32]. The value of Δ varies in a wide range in a series of terbium-containing crystals which have been studied by EPR. For instance, two types of Tb^{3+} centers of CaF_2 show $\Delta = 5.134$ and 31.67 GHz [33]; in crystals of KPb_2Cl_2:Tb $\Delta = 48$ GHz [34]; two positions of Tb^{3+} in forsterite Mg_2SiO_4 have $\Delta = 194.9$ and 235.9 GHz [35]. For main centers of Tb^{3+} in YAG this value is 81.09 GHz [23].

Energy levels scheme in Fig. 1a corresponds to those centers of Tb^{3+} in YAG which give the most intensive EPR lines. In addition to these main centers (Tb^{3+} ions in the regular environment) the spectrum contains weaker EPR lines for other types of terbium centers, labelled in Fig. 1b as Tb^{3+}(I), Tb^{3+}(II), and Tb^{3+}(III). They show the same hyperfine structure as the main centers, and their energy levels differ from that given in Fig. 1a only by the value of zero-field splitting. In the EPR spectra recorded at 130 GHz the signals of Tb^{3+}(I) overlap with the signals of Tb^{3+} and Tb^{3+}(II), as shown in Fig. 1b.

Parameters of terbium centers in YAG are listed in Table 1. It is worth noting that the zero-field splitting Δ of all additional Tb^{3+} centers in YAG are larger than for the main center type. The zero-field splitting of the ground state of different terbium centers is compared with the quantum energies at the frequencies of 94 and 130 GHz in Fig. 2a. For Tb^{3+}(I), Δ is close to the energy of the 94 GHz quantum, and for Tb^{3+}(II) and Tb^{3+}(III) the splitting exceeds the quantum energy, and hence their EPR spectra cannot be obtained at 94 GHz.

Cerium and terbium, like most of rare-earth ions, occupy the dodecahedral c-position in yttrium-aluminum garnet, substituting Y^{3+} in its lattice positions. There are six corresponding positions in YAG, and thus six EPR lines of magnetically nonequivalent centers can be observed for an arbitrary crystal orientation. This statement is true for Ce^{3+} centers, but for Tb^{3+} the situation becomes simpler since they have
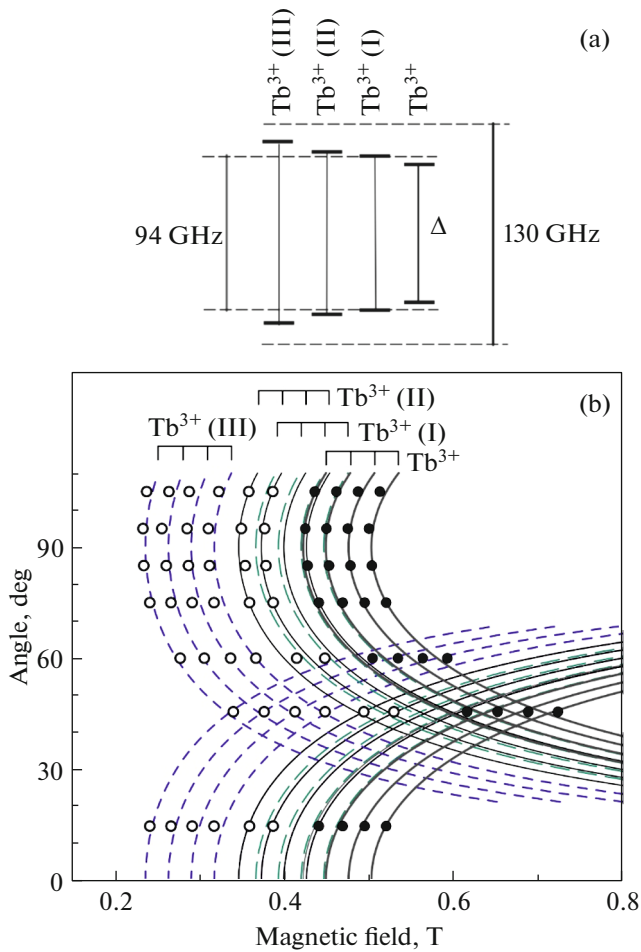
Fig. 2. (a) Comparison of the zero-field splitting of non-Kramers doublets of the main Tb^{3+} center and of the centers $Tb^{3+}(I)$, $Tb^{3+}(II)$, and $Tb^{3+}(III)$ in the YAG crystal with the energies of the microwave quanta at 94 and 130 GHz. (b) Experimental (circles) and calculated (curves) angular dependences of the EPR spectra at 130 GHz in the (100) plane for the four types of the Tb^{3+} centers.

$g_{\perp} = 0$, and only three magnetically nonequivalent terbium centers with the axial symmetry along the axis $\langle 001 \rangle$ are observed for an arbitrary crystal orientation. When the crystal is rotated in the (100) plane, only two of three magnetically nonequivalent centers are observed.

Angular dependences of the EPR spectra recorded at 130 GHz in the crystallographic plane (100) for different centers in YAG are shown in Fig. 2b. Circles present the experimental values of resonance fields, and curves are calculated from Eq. (2) according to the parameters from the table 1. Angular dependences for $Tb^{3+}(I)$, $Tb^{3+}(II)$, and $Tb^{3+}(III)$ are similar to the dependence for the main center Tb^{3+}, so these centers may be identified as Tb^{3+} ions in dodecahedral positions of the garnet lattice. Different values of the parameter Δ give an evidence of different distortions of

the crystalline field, which may appear due to defects in the environment of the terbium ions.

EPR signals of the lower intensity were also found for Ce^{3+} centers in the studied YAG:Ce, Tb crystal. Figure 3 shows a fragment of the Ce^{3+} EPR spectrum recorded at 130 GHz in the YAG:Ce, Tb crystal in the orientation near **B** ∥ [001] (curve *1*). The EPR spectrum of the YAG:Ce crystal acquired at 9.35 GHz is also shown for comparison (*2*). Magnetic field axes are scaled so that the positions of lines with the same g factors coincide in both EPR spectra registered at 9.35 and 94 GHz. Three most intensive additional lines in the spectrum (*2*) correspond to the lines in the spectrum (*1*). The lines of the satellite centers in the high-frequency spectrum (*1*) in Fig. 3 are split due to a small deviation of the sample orientation from the direction [001], since small variations of the g factor lead to significant line shifts. The g factors for these lines (g_z = 2.7 for $Ce^{3+}(I)$, 2.70 for $Ce^{3+}(II)$, and 2.67 for $Ce^{3+}(III)$) are smaller than for the cerium ions in the regular environment: g_z = 2.74. Orientation dependences of the resonance fields near the direction [001] are similar for the EPR signals of the main and additional Tb^{3+} and Ce^{3+} centers. Analogous signals in cerium EPR spectra were observed earlier in the studies of the satellite lines in YAG:Ce in the 3-cm wave range [21] and were assigned to the Ce^{3+} ions having an antisite defect Y_{Al} in their environment.

Ce^{3+} ions have one unpaired $4f$ electron. Its ground state is split due to the spin-orbital interaction and crystalline field. The ground state with the electron configuration $4f^1$ has two levels $^2F_{5/2}$ and $^2F_{7/2}$ with the gap of about 2000 cm^{-1} between them. The second and third Kramers doublets in Ce^{3+} possess high energies in YAG (228 and 587 cm^{-1}), and hence EPR transitions are observed only between the components of the lowers Kramers doublet. EPR spectra of Ce^{3+} can be described using the effective spin of $S = 1/2$ and an anisotropic g factor. Spin Hamiltonian has the form $\hat{H} = \mu_B \mathbf{S} \cdot \mathbf{g} \cdot \mathbf{B}$, where μ_B is the Bohr magneton. Parameters of the tensor **g** depend on the crystalline field in the disposition point of Ce^{3+} and are thus sensitive to changes in the nearest environment of the ion.

Cerium has no stable odd isotopes, so its EPR spectra do not show hyperfine structure which could be related unambiguously to cerium ions. The conclusion that the weak signals belonged to Ce^{3+} was made in [21] based on the similarity of the orientation and temperature dependences. In the case of Tb^{3+} ions with the nuclear spin of $I = 3/2$, the weak satellite EPR signals show a clear hyperfine structure with the same splitting as in the main terbium signals—individual Tb^{3+} ions occupying Y^{3+} positions in the regular environment. Therefore, satellite EPR signals of terbium can be reliably assigned to paramagnetic centers containing single Tb^{3+} ions.
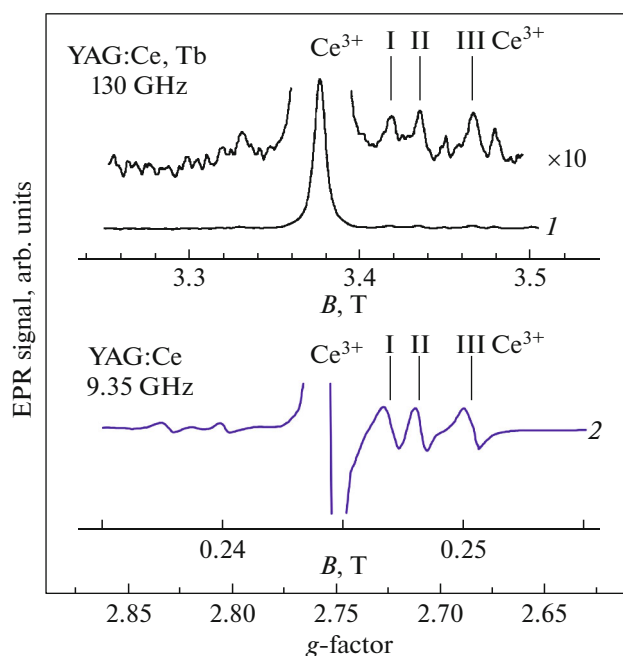
Fig. 3. EPR signals of different Ce^{3+} centers recorded at 130 GHz in the YAG:Ce, Tb crystals in the orientation close to $B \parallel [100]$ (spectrum *1*). EPR spectrum (*2*) obtained at 9.35 GHz in the YAG:Ce crystal at $T = 4.2$ K is shown for comparison.

Fig. 4. Part of the unit cell of YAG showing the distances between the dodecahedral yttrium center and closest octahedral aluminum centers.

Evidently, substitutions $Y^{3+} \rightarrow Al^{3+}$ or $Al^{3+} \rightarrow Y^{3+}$ happening near the impurity rare-earth ion Tb^{3+} or Ce^{3+} will lead to quite different distortions of oxygen polyhedra: stretching or compression, respectively. An increase in the splitting Δ for Tb^{3+} means that the O^{2-} ions shift closer to the paramagnetic center (compression of the oxygen dodecahedron). We can conclude that the observed satellite lines of terbium belong to Tb^{3+} ions associated with the $Y_{Al(a)}$ antisite defects (Y^{3+} ions replacing octahedral Al^{3+}).

To explain the amount of the additional paramagnetic centers of terbium and cerium, consider the structure of the environment of a dodecahedral center in the YAG lattice, where these ions are localized, and possible positions of the nearest antisite defects Y_{Al} occupying octahedral Al positions. It was noted above that formation of antisite defects Y_{Al} in tetrahedral centers is hardly probable. The concentration of the antisite defects is small, on the order of one per cent, hence only one antisite defects Y_{Al} is expected to be met near an impurity ion of terbium or cerium. Figure 4 shows a fragment of the unit cell of the YAG crystal with octahedral positions of aluminum ions closest to the dodecahedral yttrium center. There are 10 octahedral Al^{3+} ions sharing a common oxygen ions in the environment of the Y^{3+} position. Oxygens and tetrahedral centers of aluminum are not shown in Fig. 4 for the sake of simplicity. When Al^{3+} is substituted for Y^{3+}
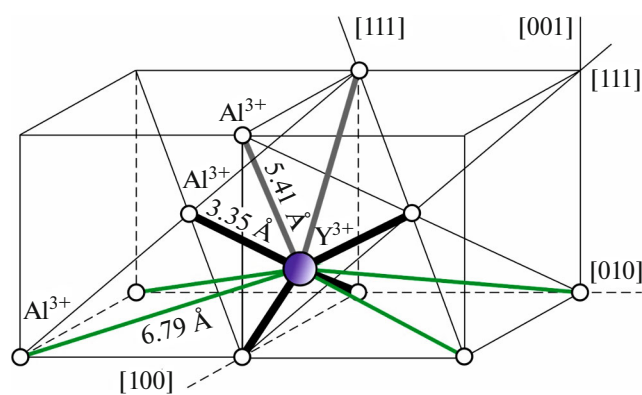
in these positions, the crystalline field in the position of the paramagnetic center will be quite large.

Thick lines in Fig. 4 show the distances between the octahedral yttrium center and octahedral positions of aluminum. The distance from the dodecahedral to the nearest octahedral centers of aluminum in YAG takes three values: 3.35, 5.41, and 6.79 Å. More distant octahedral positions are farther than 7.35 Å and do not have a common oxygen ions with the dodecahedral *c*-center. Therefore the influence of an antisite defect in that positions on the crystalline field in the dodecahedral center would be less prominent than for the ten positions closer to the *c*-center.

Three possible distances from the impurity ion of terbium or cerium to the antisite defect define three possible variants of the crystalline field distortion, leading to the changes in the zero-field splitting Δ of Tb^{3+} ions and g factor values of Ce^{3+} ions. Thus, the presence of an antisite defect near the impurity rare-earth ion of terbium or cerium should results in formation of three types of paramagnetic centers with parameters differing from the parameters of the ions in the regular environment. It agrees with the number of experimentally found additional centers of Tb^{3+} and Ce^{3+}. The strongest distortion of the crystalline field corresponds probably to the closest antisite defect at the distance of 3.36 Å from the Tb^{3+} (Ce^{3+}) ion. Centers Tb^{3+}(III) and Ce^{3+}(III) show the largest deviations of the parameters from the regular values. The smallest changes in Δ and g factor observed for the centers Tb^{3+}(I) and Ce^{3+}(I) correspond to the antisite defects at the distance of 6.79 Å from Y^{3+}.

Concentration of the Tb^{3+} and Ce^{3+} ions having an antisite defect in their vicinity in the investigated YAG:Ce, Tb crystal was estimated by comparing the EPR line intensities of these centers and of the Tb^{3+} and Ce^{3+} ions occupying dodecahedral centers in the regular environment. EPR spectra presented in Fig. 1 show that about 6% of terbium ions are close to the

antisite defect, since the EPR signal intensity of each of the centers $Tb^{3+}(I)$, $Tb^{3+}(II)$, and $Tb^{3+}(III)$ is about 2% of the Tb^{3+} EPR line intensity. A similar ratio is observed for the cerium centers. This result agrees with the estimate made for the YAG:Ce crystal in [21]. As mentioned above, the antisite defect Y_{Al} causing changers in the EPR spectral parameters can be found in one of every ten octahedral positions of Al^{3+} in the environment of the impurity ion Tb^{3+} or Ce^{3+}; thus, the concentration of antisite defects in the studied crystal is approximately 0.6%.

CONCLUSIONS

We can conclude that the nature of additional paramagnetic centers of cerium and terbium in YAG crystals is the same: they appear due to the presence of antisite defects Y_{Al} in the vicinity of the impurity ions. In both cases EPR spectra of associates of the rare-earth ions of Tb^{3+} and Ce^{3+} with the antisite defects Y_{Al} (where yttrium replaces aluminum in the octahedral centers of the YAG lattice) are observed together with the main signals of Tb^{3+} and Ce^{3+} ions occupying dodecahedral centers in the YAG lattice in the regular environment.

CONFLICT OF INTEREST

Authors declare that they have no conflicts of interest.

REFERENCES

1. A. Kaminskii, *Laser Crystals. Their Physics and Properties* (Springer, Berlin, 1990).
2. V. Bachmann, C. Ronda, and A. Meijerink, Chem. Mater. **21**, 2077 (2009).
3. Y. S. Lin, R. S. Liu, and B.-M. Cheng, J. Electrochem. Soc. **152**, J41 (2005).
4. A C. Dujardin, E. Auffray, E. Bourret-Courchesne, P. Dorenbos, P. Lecoq, M. Nikl, A. N. Vasil'ev, A. Yoshikawa, and R. Zhu, IEEE Trans. Nucl. Sci. **65**, 1977 (2018).
5. P. Slyushev, K. Xia, R. Reuter, M. Jamali, N. Zhao, N. Yang, C. Duan, N. Kukharchyk, A. D. Wieck, R. Kolesov, and J. Wrachtrup, Nat. Commun. **5**, 3895 (2014).
6. S. Geller, G. P. Espinosa, L. D. Fullmer, and P. B. Crandall, Mater. Res. Bull. **7**, 1219 (1972).
7. M. K. Ashurov, Y. K. Voronko, V. Osiko, A. Sobol, and M. Timosheckin, Phys. Status Solidi A **42**, 101 (1977).
8. Kh. S. Bagdasarov, E. A. Fedorov, V. I. Zhekov, and V. A. Lobachev, Tr. IOFAN **19**, 112 (1989).
9. J. Dong and K. Lu, Phys. Rev. B **43**, 8808 (1991).
10. C. Landron, S. Lefloch, M. Gervais, J. P. Coutures, and D. Bazin, Phys. Status Solidi B **196**, 25 (1996).
11. P. Novak, J. Englich, H. Stepankova, J. Kohout, H. Luetgemeier, K. Wagner, and W. Tolksdorf, J. Phys. IV (Paris) **7**, C1-283 (1997).
12. V. Babin, V. Gorbenko, I. Kondakova, T. Karner, V. V. Laguta, M. Nikl, S. Zazubovich, and Yu. Zorenko, J. Phys. D **44**, 315402 (2011).
13. M. M. Kuklja and R. Pandey, J. Am. Ceram. Soc. **82**, 2881 (1999).
14. M. M. Kuklja, J. Phys.: Condens. Matter **12**, 2953 (2000).
15. Bo Liu, Mu Gu, Xiaolin Liu, Shiming Huang, and Chen Ni, Appl. Phys. Lett. **94**, 121910 (2009).
16. A. B. Munoz-Garcia, E. Artacho, and L. Seijo, Phys. Rev. B **80**, 014105 (2009).
17. A. B. Munoz-Garcia, Z. Barandiaran, and L. Seijo, J. Mater. Chem. **22**, 19888 (2012).
18. M. Nikl, V. V. Laguta, and A. Vedda, Phys. Status Solidi B **245**, 1701 (2008).
19. C. R. Stanek, K. J. McClellan, M. R. Levy, C. Milanese, and R. W. Grimes, Nucl. Instrum. Methods Phys. Res., Sect. A **579**, 27 (2007).
20. H. R. Lewis, J. Appl. Phys. **37**, 739 (1966).
21. G. R. Asatryan, D. D. Kramushchenko, Yu. A. Uspenskaya, P. G. Baranov, and A. G. Petrosyan, Phys. Solid State **56**, 1150 (2014).
22. V. V. Laguta, A. M. Slipenyuk, M. D. Glinchuk, I. P. Bykov, Y. Zorenko, M. Nikl, J. Rosa, and K. Nejezchleb, Rad. Meas. **42**, 835 (2007).
23. E. V. Edinach, Y. A. Uspenskaya, A. S. Gurin, R. A. Babunts, H. R. Asatryan, N. G. Romanov, A. G. Badalyan, and P. G. Baranov, Phys. Rev. B **100**, 104435 (2019).
24. Kh. S. Bagdasarov, in *Modern Crystallography*, Ed. by B. K. Vainshtein (Nauka, Moscow, 1980), Vol. 3, p. 337 [in Russian].
25. A. G. Petrosyan, J. Cryst. Growth **139**, 372 (1994).
26. A. G. Petrosyan, G. O. Shirinyan, K. L. Ovanesyan, and A. A. Avetisyan, Krist. Technol. **13**, 43 (1978).
27. B. Cockayne, J. M. Roslington, and A. W. Vere, J. Mater. Sci. **8**, 382 (1973).
28. A. A. Chernov, Cryst. Ann. Rev. Mater. Sci. **3**, 373 (1973).
29. A. G. Petrosyan, K. L. Ovanesyan, R. V. Sargsyan, G. O. Shirinyan, D. Abler, E. Auffray, P. Lecoq, C. Dujardin, and C. Pedrini, J. Cryst. Growth **312**, 3136 (2010).
30. A. G. Petrosyan and G. O. Shirinyan, Neorg. Mater. **29**, 258 (1993).
31. E. V. Edinach, Yu. A. Uspenskaya, A. S. Gurin, R. A. Babunts, G. R. Asatryan, N. G. Romanov, A. G. Badalyan, and P. G. Baranov, Phys. Solid State **61**, 1820 (2019).
32. A. Abragam and B. Bleaney, *Electron Paramagnetic Resonance of Transition Ions* (Oxford Univ., London, 1970).
33. P. A. Forrester and C. F. Hempstead, Phys. Rev. **126**, 923 (1962).
34. G. S. Shakurov, B. Z. Malkin, A. R. Zakirov, A. G. Okhrimchuk, L. N. Butvina, N. V. Liehkova, and V. N. Zavgorodnev, Appl. Magn. Res. **26**, 579 (2004).
35. A. A. Konovalov, D. A. Lis, K. A. Subbotin, V. F. Tarasov, and E. V. Zharikov, Appl. Magn. Res. **45**, 193 (2014).

Translated by S. Efimov